Journal of Innovative Materials in Extreme Conditions
2026
Volume 7
Issue 1

HIGH PRESSURE/HIGH-TEMPERATURE BEHAVIOR AND PHYSICAL PROPERTIES OF COMPOSITIONALLY COMPLEX CARBONITRIDES

Dharma Teja TEPPALA,[1,3] Shrikant BHAT,[2] Anke WEIDENKAFF,[3] Marc WIDENMEYER,[3] Emanuel IONESCU[1,*]

[1] *TU Wien, Institute for Chemical Technologies and Analytics, Getreidemarkt 9, 1060 Wien, Austria*
[2] *Deutsches Elektron Synchrotron, Notkestrasse 85, D-22607 Hamburg, Germany*
[3] *TU Darmstadt, Institute for Materials Science, Peter-Grünberg-Str. 2, D-64287 Darmstadt, Germany*
[*] *Corresponding author: Emanuel Ionescu (emanuel.ionescu@tuwien.ac.at)*

Abstract: *Compositionally complex carbides, nitrides, and carbonitrides represent a promising class of ceramics stable under high temperatures, high pressures, and ultra-harsh environmental conditions. However, their structural stability under simultaneous high-pressure and high-temperature conditions remains largely unexplored. To address this, in this work, two single-phase ceramic compositions, i.e., (Ti,Zr,Hf,Nb,Ta)$C_{0.54}N_{0.4}$, (V,Nb,Ta,Mo,W)$C_{0.8}$, were synthesized through non-oxidic sol-gel assisted high temperature annealing, resulting in phase pure powders with tailored anionic compositions confirmed by elemental analysis. The phase evolution, possible phase transformations, and phase stability were examined using an in-situ high-pressure-high-temperature method up to 20 GPa and 1900 °C. Both compositions remained structurally stable throughout the investigated pressure-temperature range, and the bulk modulus of these compositions was determined to be 309 GPa and 267 GPa using the Birch-Murnaghan EOS under room-temperature compression, exceeding those of the binary constituents. At 20 GPa, both ceramics exhibited anharmonic volumetric thermal expansion behavior described by* $\boldsymbol{\alpha_V^{20}}$ *= 5.97*10^{-6}+1.33*10^{-8}T,* $\boldsymbol{\alpha_V^{20}}$ *= 2.84*10^{-6}+2.05*10^{-8}T, respectively. The coefficient of thermal expansion of (Ti,Zr,Hf,Nb,Ta)$C_{0.54}N_{0.4}$ at ambient pressure was determined to be 2.58*10^{-5} /K up to 600 °C.*

1. Introduction

Early transition-metal compositionally complex carbides, nitrides, and carbonitrides represent an important class of ceramics that has attracted considerable attention due to their remarkable combination of properties compared to their binary constituents [1-5]. The improved properties of compositionally complex ceramics are generally attributed to the so-called „core effects", *i.e.*, high configurational entropy, sluggish diffusion, lattice distortion, and synergistic effects, which were initially described by Jin Wei Yeh for high-entropy alloys [6] and later extended to ceramics following the synthesis of the first compositionally complex oxide, (Mg,Co,Cu,Ni,Zn)O, by Rost [7].

Due to their remarkable structural stability, oxidation resistance, high-temperature mechanical performance, and hardness, early transition-metal compositionally complex ceramics containing group IVB, VB, and VIB cations are often classified as ultra-high-temperature ceramics (UHTCs). These materials typically possess melting points above 3000 °C and generally crystallize in a cubic rock-salt structure consistent with most binary counterparts [8-10].
Typically, the synthesis of such ceramics requires temperatures as high as 1700 °C and pressures around 100 MPa to obtain dense samples. Spark plasma sintering is commonly employed to fabricate these ceramics in specific shapes through reaction sintering of oxides or consolidation of single-phase ceramic powders [11-15]. Such powders are frequently produced using sol–gel [16-19], polymer-derived [20-21], or molten salt methods [22-24]. Although the synthesis and mechanical properties of compositionally complex carbides, nitrides, and carbonitrides have been extensively investigated, with hardness, elastic modulus, and fracture toughness values well documented [25-27], there remains limited research on their structural stability under high-pressure conditions.
Initial studies by Guan et al. [28-29] on the high-pressure synthesis of (Ti,Zr,Nb,Ta,Mo)C and (Ti,Zr,Hf,Nb,Ta)C have provided important insights into carbide stability under hydrostatic and non-

hydrostatic conditions, including possible phase transformations and room-pressure bulk modulus determination. Similarly, studies on (V,Nb,Ta,Mo,W)C under cold compression by Iwan et al. [31] using diamond anvil cells up to 70 GPa revealed exceptional incompressibility, with bulk moduli exceeding 350 GPa. These findings were further supported by similar studies conducted by Shu et al. [32] up to 58.4 GPa.

In the present work, two compositionally complex systems, namely (Ti,Zr,Hf,Nb,Ta)C_xN_{1-x} and (V,Nb,Ta,Mo,W)C_x, were synthesized via a non-oxidic sol–gel route followed by high-temperature annealing. The resulting materials were investigated using *in situ* energy-dispersive X-ray diffraction (ED-XRD) under pressures up to 20 GPa and temperatures up to 1900 °C in a large-volume press (LVP). The structural stability, phase evolution, and compressibility of these systems were systematically analyzed, and their bulk moduli were determined using the Birch–Murnaghan equation of state. These findings provide new insights into the stability and mechanical response of compositionally complex carbonitrides under high-pressure and high-temperature conditions and contribute to the broader understanding of high-entropy ceramic systems.

In this context, in situ high-pressure X-ray diffraction techniques provide powerful tools for probing structural evolution and extracting equation-of-state parameters under relevant conditions. Energy-dispersive X-ray diffraction (ED-XRD) enables rapid data acquisition over a wide energy range, making it particularly suitable for experiments involving dynamic temperature and pressure variations.

2. Experimental

2.1. Sample Preparation

High-purity commercial $TiCl_4$, $ZrCl_4$, $HfCl_4$, $NbCl_5$, $TaCl_5$, $MoCl_5$, WCl_6, $LiN(CH_3)_2$, and n-hexane were purchased from Merck (Germany) and stored in a glovebox to avoid oxygen contamination. n-Hexane was used as received without further purification. All glassware used for the non-oxidic sol-gel synthesis, including low-temperature ammonolysis, was oven-dried at 120 °C for at least 1 day to remove adsorbed moisture, and all synthetic procedures were performed using a Schlenk line setup.

Two compositions corresponding to (Ti,Zr,Hf,Nb,Ta) and (V,Nb,Ta,Mo,W) were prepared via the non-oxidic sol-gel process, with the detailed synthesis method reported elsewhere [36,37]. Briefly, equimolar amounts of the respective metal precursors of the combination were added to the suspension containing stoichiometric lithium dimethylamide in 200 mL of n-hexane. After refluxing for 4 h at 70 °C, the reaction mixture was filtered in inert gas atmosphere for the removal of LiCl. The resulting metal dimethylamide solution was subsequently subjected to low-temperature ammonolysis at -100 °C using a cold bath, yielding a precipitated xerogel. The ammonolysis setup was warmed to room temperature overnight under an argon atmosphere. Subsequently, n-hexane was removed by vacuum evaporation, yielding the xerogel, which was stored in a glovebox for further use due to its air and moisture sensitivity.

The xerogel was then subjected to high-temperature ammonolysis at 1000 °C for 3 h under high-purity NH_3 (≥99.999%), with a ramp rate of 200 °C/h during heating and cooling to obtain nitrides. Furthermore, the nitrides were annealed in a graphite crucible at 1700 °C for 3 h under N_2 with a ramp rate of 20 °C/min during heating and cooling to obtain carbonitrides. The resulting carbonitrides were subsequently subjected to high-pressure and high-temperature conditions to evaluate their structural stability and determine key physical properties, e.g., bulk modulus and thermal expansion coefficients.

2.2 Characterization techniques

The xerogel was analyzed using a Fourier-transform infrared spectrometer (FTIR) in attenuated total reflection (ATR) under an argon atmosphere with a VARIAN-670 (Agilent

Technologies) in the range of 500 cm-1 to 4000 cm-1, with automatic baseline and background corrections.
The crystal structure and the phase composition details were obtained from XRD patterns recorded in transmission mode with STOE STADI-MP (STOE and Cie GmbH, Darmstadt, Germany) equipped with a Germanium (111) monochromator, resulting in Mo-$K_{\alpha 1}$ radiation (λ=0.70932 Å), with a step size of 0.105° and with an acquisition time of 30 s per step.
In-situ HT XRD measurements on the carbonitride of group IV-V were performed using a customized setup from STOE GmbH (STOE and Cie GmbH, Darmstadt, Germany), with a Ge (111) monochromator, resulting in Mo-Ka1 (λ = 0.70932Å) and a 670.3 heating device (shielded from air by Kapton) from Huber Diffraktionstechnik GmbH and Mythen 2K detector from DECTRIS. The measurement was performed by filling the powder into a 0.5 mm-diameter quartz capillary and sealing it with epoxy. The powder was loaded into a 0.5 mm diameter quartz capillary and sealed with epoxy. The setup was heated at 20 °C/min, with an acquisition time of 2 h per measurement at selected temperatures.
The diffractograms were analyzed using MATCH! software (Crystal Impact GmbH, Germany), while the Rietveld refinements of ambient-condition phases were performed using Fullprof version 7.95 [38] with Thompson Cox and Hastings, with the Axial Divergence function using 7-coefficient Chebyshev polynomials. NIST SRM 660b LaB_6 was employed to determine the zero shift and instrumental contribution within the diffraction patterns. For HT-XRD, the Pseudo-Voigt function was chosen, with linear interpolation of background points.
The carbon content of the pre-HP-HT ceramics was determined through combustion analysis (LECO C-200, LECO Instruments GmbH, Germany), while the O and N analysis was performed using ELEMENTRAC ONH-p2 analyzer (Eltra elemental analyzers, Verder Scientific, Haan, Germany).
The morphology of the post HP-HT ceramics was investigated using a scanning electron microscope JSM-7600F (JEOL Ltd., Tokyo, Japan). The morphology of the pre-HP-HT ceramics was examined using a Phillips XL30 FEG high-resolution scanning electron microscope (FEI Company, Hillsboro, Oregon, USA) and an energy-dispersive X-ray spectroscope (EDS; Mahwah, New Jersey, USA).

2.3 High-Pressure/High-Temperature Setup

In-situ XRD experiments under high-pressure and high-temperature conditions were conducted using a 6-8 Kawai-type compression geometry with a Hall-type six-ram LVP (Mavo press LPQ6 1500-100, Max Voggenreiter GmbH, Germany) at the P61B beamline at DESY, Hamburg.
Tungsten carbide (WC) second-stage anvils (32mm, FUJILLOY TF08, Japan) with a truncated edge of 4 mm were used to compress the Cr_2O_3-doped MgO octahedron, with an edge length of 10 mm. The Cr_2O_3-doped MgO octahedron assembly was used as a pressure-transmission medium, together with a TiB_2 cylindrical heater (EBN grade, Denka Japan, Japan).
The precursor powders were hand-pressed into a cavity within a metal disc (height (h) = 1.4 mm, diameter (ϕ) = 1.8 mm) inside the glovebox and subsequently placed into an h-BN tube to prevent exposure to air or moisture. Similarly, mixtures of Pt+KCl, or MgO+CsCl, were prepared and loaded into a h-BN tube as real-time pressure markers. The sample and the pressure marker were simultaneously loaded into the octahedron. Additional details of the experimental setup are provided elsewhere [35]. For pressure determination, Yokoo EOS [36] was applied to Pt, Tateno EOS [37] for B2-KCl (B1-B2 transformation occurs at 2 GPa), Tange-Vinet for MgO [38], and Dewaele for CsCl [39].

Prior to the experiments, detector energy calibration was performed using ^{57}Co and ^{133}Ba radionuclide sources. The positions of the two Ge detectors (with Pb shielding) were calibrated to 4.9615° (2θ) and 3° (2θ), respectively, using a LaB_6 standard (National Institute of Standards and Technology (NIST) SRM 660c). Diffracted X-rays from the sample were collected over an energy range of 20–160 keV.

The assembly was initially compressed to a target pressure of 20 GPa at room temperature and subsequently heated stepwise to approximately 1900 °C to investigate the structural stability of the compositionally complex carbonitrides under combined pressure and temperature conditions. ED-XRD patterns were recorded during heating at different temperatures up to ca. 1900 °C (rounded—

calculated values of ±20 °C based on a calibrated power-temperature relationship), only after the temperature had reached a steady state during each heating step. The ED-XRD patterns were visualized using PDIndexer [40], and lattice parameters were accurately determined through Le Bail refinement using the General Structure Analysis System (GSAS-II) [45]. The room pressure compression data were fitted using EoSFit software [46].

3. Results and Discussion

3.1 Compositionally Complex Carbonitrides- Pre-compression.

The xerogel obtained via low-temperature transamination was investigated by means of FTIR spectroscopy, and the corresponding spectrum is shown in Figure 1. The presence of bands corresponding to N-H vibrations centered at 3300 cm^{-1} as well as of M-N deformations at 1150 cm^{-1} - 950 cm^{-1} confirms transamination with ammonia. However, the presence of CH_3 vibrational bands centered at 2900 cm^{-1} and NC_2 deformation bands at 960 cm^{-1} indicates that transamination was only partially complete. [32,33] The xerogel was obtained as a solid precipitate from n-hexane during transamination, suggesting partial macromolecular network formation and a certain degree of M–N-mediated crosslinking.

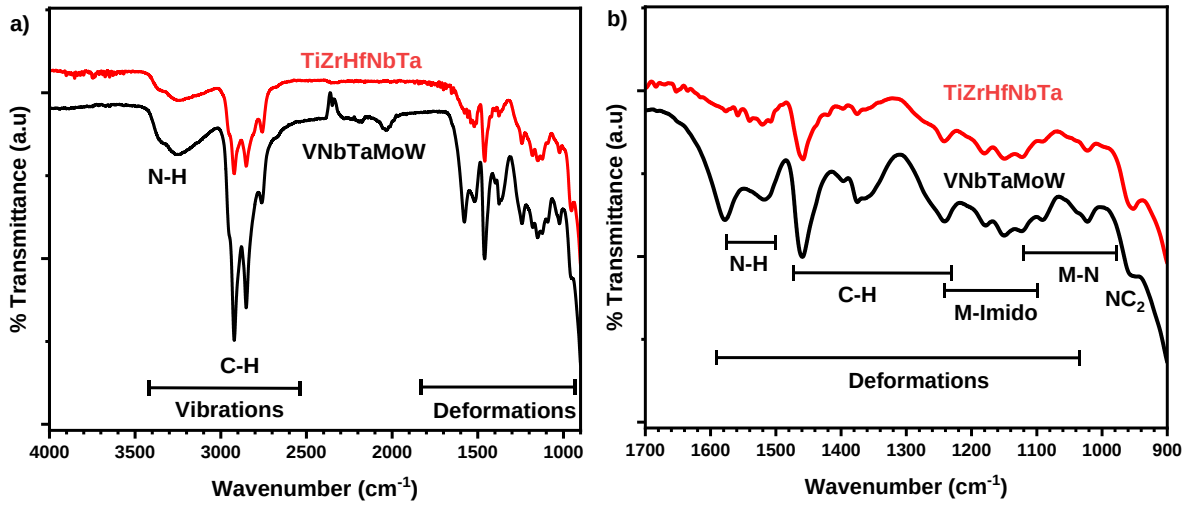

Figure 1. (a) FTIR-ATR spectra of the xerogels, (b) Inset of the spectrum in the fingerprint area.

The ceramics obtained after ammonolysis at 1000 °C and subsequent annealing at 1700 °C were evaluated by XRD to identify phase composition and structural evolution. For the (Ti,Zr,Hf,Nb,Ta) system, the diffractogram of the ceramic obtained at 1000 °C exhibits high intensity peaks corresponding to (111), (200), (220), (311), and (222) planes of rock-salt structure at 2θ = 16.5°, 19.1°, 27.1°, and 31.9° respectively and can be seen in Figure 2a. However, several weak additional reflections indicate the presence of minor secondary phases. Many of the weak reflections of the potential minor phases are indexed to ZrO_2-based oxides, primarily monoclinic ($P2_1/c$), likely resulting from oxygen contamination during sample handling. The lattice parameter of the nitride phase is determined to be 4.26(1) Å.

Following annealing at 1700 °C, the diffractogram showed the disappearance of oxide-related minor peaks. Thus, the ceramic was observed to be single-phase and determined to be of rock-salt structure, with the diffraction peaks shifting to lower angles. These observations suggest carbothermal reduction of oxide phases and carbon incorporation into the anionic sublattice, reflected by an increased lattice parameter of 4.39(1) Å. Elemental analysis confirmed that the sample annealed at 1000 °C was predominantly a nitride, whereas the sample annealed at 1700 °C formed a carbonitride with the composition $(Ti,Zr,Hf,Nb,Ta)C_{0.54}N_{0.4}$.

While the (Ti,Zr,Hf,Nb,Ta) system yielded well-crystallized ceramics, the (V,Nb,Ta,Mo,W) system exhibited distinct behavior (Figure 2b). Elemental analysis revealed that the 1000 °C ceramic was a pure nitride, whereas the 1700 °C annealed ceramic consisted exclusively of carbon. The diffractogram of the sample obtained at 1000 °C displayed significantly broadened reflections characteristic of a rock-salt structured phase, indicating substantial lattice strain and nano-crystallinity. Minor low-intensity reflections at lower angles suggest the presence of oxide impurities, although these were insufficiently intense for unambiguous phase identification. After annealing at 1700 °C, a similar diffractogram with sharper reflections was observed, indicating the formation of a carbide phase with the composition (V,Nb,Ta,Mo,W)C_x (x = 0.8). The lattice parameters were determined to be 4.22(1) Å and 4.35(1) Å, for the nitride and carbide phase, respectively. The absence of nitrogen in the sample annealed at 1700 °C clearly point toward the thermodynamic instability of the nitride phase at elevated temperatures, particularly in comparison with the more stable (Ti,Zr,Hf,Nb,Ta)N-based system. Rietveld refinements for (Ti,Zr,Hf,Nb,Ta)$C_{0.54}N_{0.4}$ and (V,Nb,Ta,Mo,W)$C_{0.8}$ are presented in Figures 2c and 2d. Due to the absence of the oxidic minor phases and other secondary phases, (Ti,Zr,Hf,Nb,Ta)$C_{0.54}N_{0.4}$ and (V,Nb,Ta,Mo,W)$C_{0.8}$ were selected for subsequent high-pressure experiments. The compositions (Ti,Zr,Hf,Nb,Ta)$C_{0.54}N_{0.4}$ and (V,Nb,Ta,Mo,W)$C_{0.8}$ are labelled as BT-648, BT-649. The fit corresponding Rietveld refinement fit parameters are summarized in Table 1.

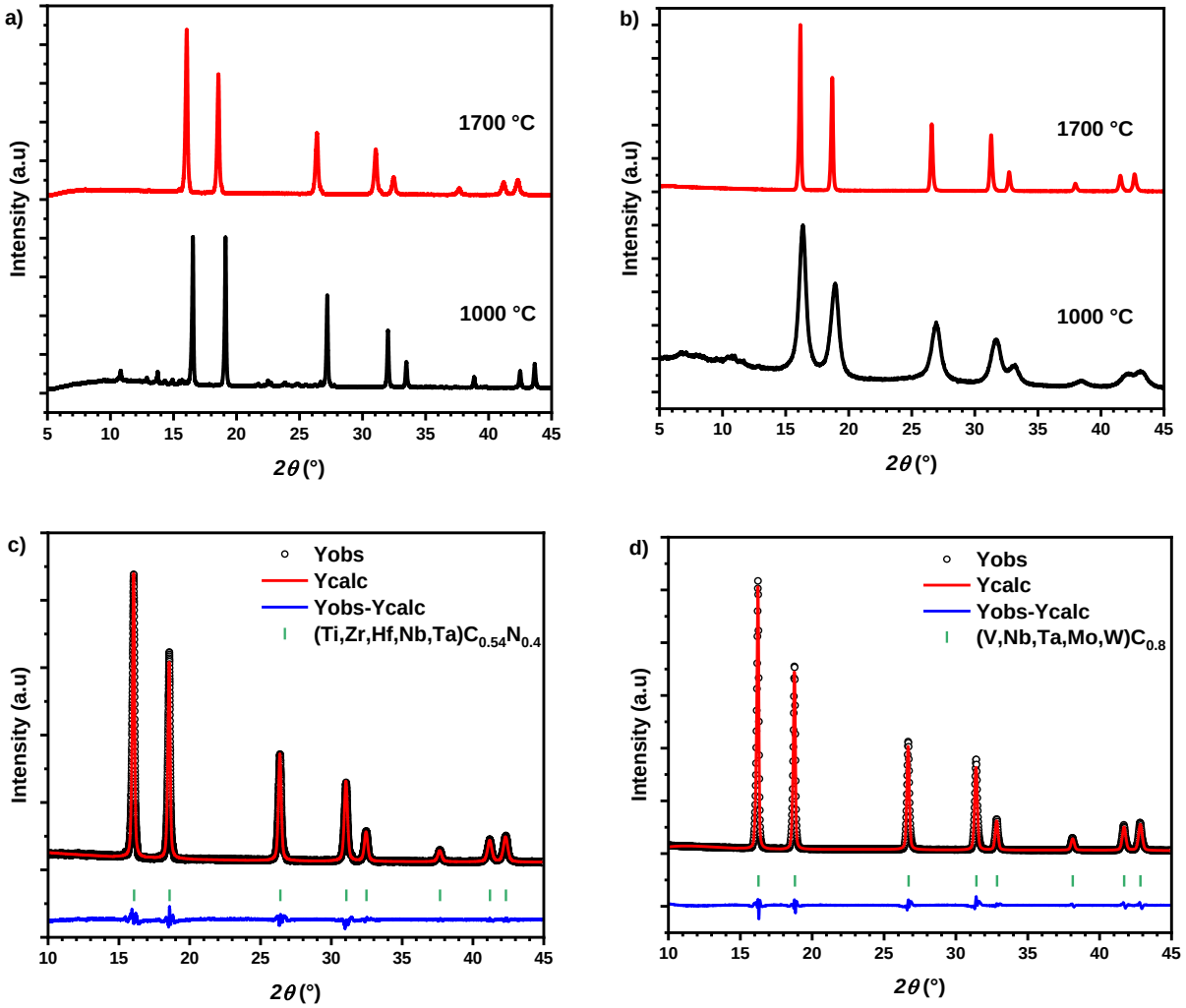

Figure 2. Diffractograms of (a) (Ti,Zr,Hf,Nb,Ta), (b) (V,Nb,Ta,Mo,W), at 1000 °C, and 1700 °C, (c) Rietveld of (Ti,Zr,Hf,Nb,Ta)$C_{0.54}N_{0.4}$ (BT-648), (d) Rietveld of (V,Nb,Ta,Mo,W)$C_{0.8}$ (BT-649)

Table 1. Fit parameters of Rietveld refinement for $(Ti,Zr,Hf,Nb,Ta)C_{0.54}N_{0.4}$ and $(V,Nb,Ta,Mo,W)C_{0.8}$

Sample	Rw (%)	wRp (%)	Re (%)	χ^2
$(Ti,Zr,Hf,Nb,Ta)C_{0.54}N_{0.4}$	10.3	10.2	3.96	6.66
$(V,Nb,Ta,Mo,W)C_{0.8}$	8.18	9.54	3.45	7.65

3.2 HP-HT – Compression and mechanical response

The ED-XRD patterns of BT-648 and BT-649, recorded at selected pressures during room-temperature compression, are shown in Figure 3a and 3b. As pressure increases, interatomic distances between cations and anions decrease relative to ambient conditions, resulting in lattice contraction and a corresponding shift of the diffraction peaks toward higher energies in the ED-XRD patterns.

Compression at elevated pressures can significantly influence crystal structure through lattice distortion, preferred orientation changes, and the generation of structural defects such as dislocations [39], as reflected by peak broadening and intensity variations. The intensity ratio between the (200) and (111) reflections of pre-compressed BT-648 differs between ED-XRD data (Figure 3a) and laboratory Mo-anode data (Figure 2c), which is attributed to differences in beam characteristics and experimental geometry.

With increasing pressure, the diffraction pattern gradually shifted to higher energies and exhibited increasing peak broadening, particularly at higher diffraction angles. This broadening likely arises from structural deformations and inhomogeneous strain associated with different crystal-plane responses, indicating increased dislocation density.

In addition to the characteristic diffraction peaks of the rock-salt structure, several stationary peaks were observed in the ED-XRD patterns (Figures 3c and 3d). These peaks correspond to X-ray fluorescence emissions from heavy elements such as Hf, Ta, and W present in the ceramics [42].

Similarly, Pb fluorescence peaks originating from shielding material were detected, consistent with previous instrumental observations [35]. Despite significant peak broadening and progressive lattice contraction with increasing pressure, the absence of new diffraction peaks or pronounced asymmetry indicates that both ceramics retained their rock-salt structure without detectable phase transformation up to 20 GPa.

The Le Bail fitting of BT-649 at 13.4 GPa is shown in Figure 3e as a representative example of the fitting procedure applied across the full dataset.

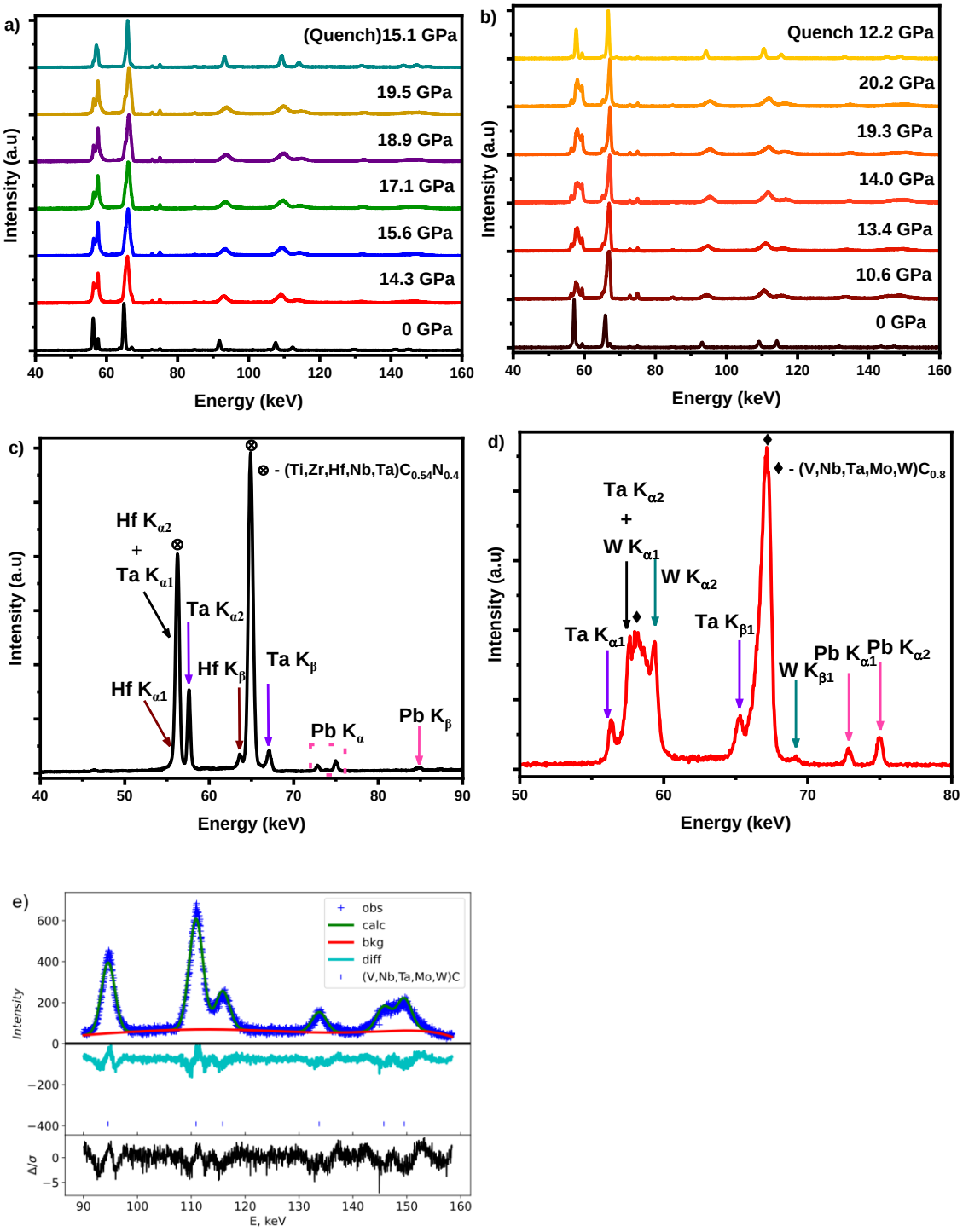

Figure 3. ED-XRD patterns of (a) BT-648, (b) BT-649, (c) BT-648 at ambient conditions, indicating fluorescence lines of Hf, Ta, (d) BT-649 at 10.6 GPa clearly showing the fluorescence lines of Ta, W, and Pb, (e) Le Bail fit of BT-649 diffractogram corresponding to 13.4 GPa.

Following confirmation of structural stability, the unit cell parameters obtained from the Le Bail fitting of the room-temperature compression dataset were plotted as a function of pressure (Figures 4a and 4b). To determine the bulk modulus, the pressure-volume data were fitted using the third-order Birch-Murnaghan equation of state, as described by Equation 1.

$$P = 1.5 * B_0 \left[\left(\frac{V_0}{V}\right)^{\frac{7}{3}} - \left(\frac{V_0}{V}\right)^{\frac{5}{3}} \right] \left\{ 1 + \frac{3}{4}(B_0' - 4)\left(\left(\frac{V_0}{V}\right)^{\frac{2}{3}} - 1 \right) \right\} \quad (1)$$

$$f_E = \frac{1}{2}\left[\left(\frac{V_0}{V}\right)^{\frac{2}{3}} - 1 \right] \quad (2)$$

$$F_E = B_0 \left[1 + \frac{3}{2}(B_0' - 4) f_E \right] \quad (3)$$

$$F_E = \frac{P}{3 f_E (1 + 2 f_E)^{\frac{5}{2}}} \quad (4)$$

where P is Pressure, V_0 (later V_{300}) is the volume at room pressure and room temperature, V denotes volume during room temperature compression, B_0 denotes ambient pressure bulk modulus, B_0' is the pressure derivative of bulk modulus, f_E represents Eulerian strain and F_E represents normalised pressure. The refinement yielded B_0 values of 309(6) GPa and 267(5) GPa in the case of BT-648 and BT-649, respectively. In both cases, B_0' was fixed at 4(0), effectively reducing the model to a 2nd order Birch- Murnaghan equation of state. The validity of the fitting procedure was also evaluated using an Eulerian strain (eq. 2) vs normalized pressure (eq. 3, 4) plot. As shown in Figures 4c and 4d, the data are best described by a line with approximately slope 0, consistent with the applicability of a 2nd-order Birch- Murnaghan equation of state.

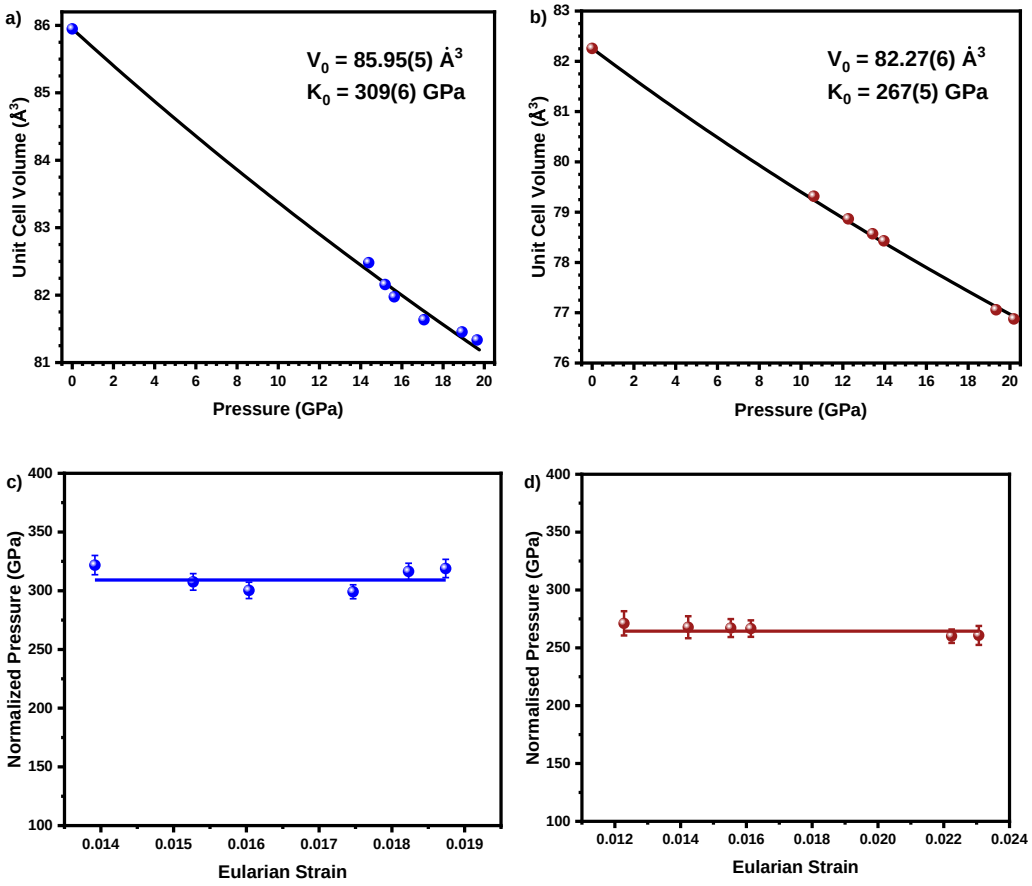

Figure 4. Birch Murnaghan 3rd order EoS fitting (K' is fixed as 4) of (a) BT-648, (b) BT-649, Eulerian strain vs normalized pressure fitting of (c) BT-648, (d) BT-649.

The experimental stress state and deformation behavior can be determined through the diffractograms. In contrast to DAC experiments, LVP conditions are generally considered quasi-hydrostatic because

pressure is applied in a tri-axial rather than uni-axial manner. As seen in Figure 5, the planar compression behavior during decompression follows similar trends across different crystallographic planes, indicating near-hydrostatic conditions throughout the experiment.

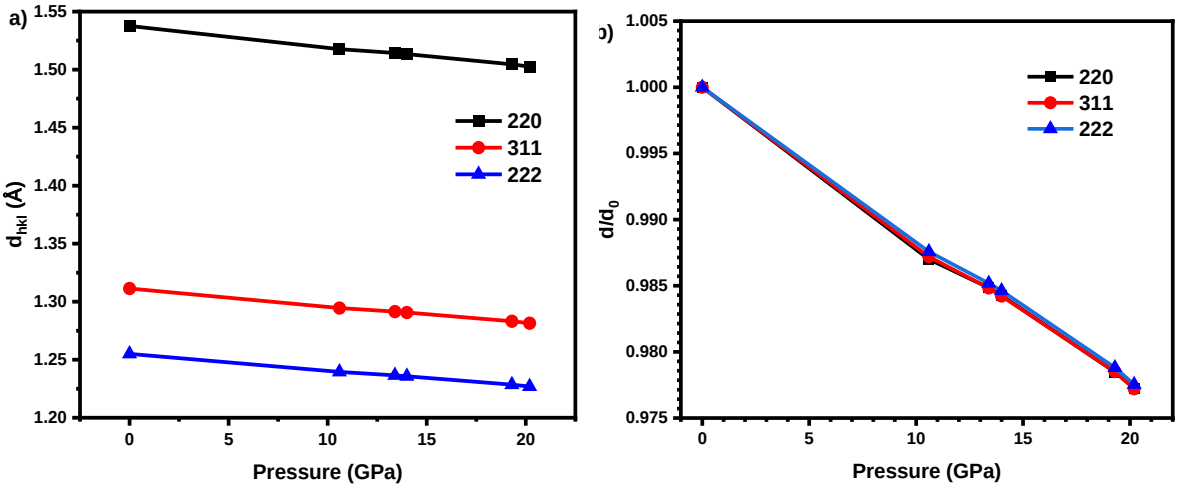

Figure 5. Reduction of the lattice parameters of BT-649 with respect to pressure (b) Trend of reduction per $d_{0(hkl)}$.

The bulk modulus values of 309 GPa, and 267 GPa for BT-648, and BT-649, respectively, exceed those reported for many binary carbides and nitrides listed in Table 2, including TiC [43,44], TiN [52], ZrC [45], HfC [44,46], NbC [48], VC[47], while remaining comparable to values reported for TaC [28], VN [54]. This deviation from binary systems is likely associated with local lattice strain fields generated by the multicomponent cation distribution under hydrostatic compression. Similar behavior has been reported for other compositionally complex carbides, e.g., (Hf,Nb,Ta,Ti,W)C (B = 291 GPa) [25], (Nb,Ta,Ti,V,W)C (253 GPa) [25], (Ti,Zr,Nb,Ta,Mo)C (311-332 GPa)[28].

Table 2. Bulk modulus of the carbides and nitrides obtained through high-pressure, high-temperature methods.

Sample	**Bulk Modulus (GPa)**	**Pressure mode**
TiC	248 [44], 282 [45]	LVP [44], DAC [45]
ZrC	210 [46]	DAC [46]
HfC	286 [45], 270 [47]	DAC [45], LVP [47]
$VC_{0.8}$	258 [48]	DAC [48]
NbC	274 [49]	DAC [49]
TaC	345 [28], 355 [47], 433 [50]	DAC [28],[50] LVP [47]
Mo_2C	307 [55]	DAC [55]
W_2C	347 [56]	DAC [56]

TiN	320 [57]	DAC [57]
Hf_3N_4	250 [58]	DAC [58]
VN	328 [59]	DAC [59]
TaN	280-320 [56]	DAC [56]
$(Ti,Zr,Nb,Ta)C_{0.8}N_{0.2}$	248 [57]	DAC [57]
(Hf,Nb,Ta,Ti,W)C	291 [25]	N.I [25]
(Hf,Nb,Ta,Ti,Zr)C	235 [25], 333 [29], 205 [58]	N.I [25], Acoustic [58]
(Hf,Nb,Ta,Ti,V)C	267 [25]	N.I [25]
(Nb,Ta,Ti,V,W)C	253 [25]	N.I [25]
(Ti,Zr,Nb,Ta,Mo)C	311-332 [28]	DAC[28]
(Hf,Ta,Ti,W,Zr)C	246 [25]	N.I [25]
(Hf,Nb,Ta,Ti,Zr)N	216 [58]	Acoustic [58]
(V,Nb,Ta,Mo,W)C	334 [31], 278 [25]	DAC [31], N.I[25]
(Ta,Nb,Hf,Zr,V)C	311[59]	DAC [59]
(Ti,Zr,Hf,Nb,Ta)CN	258 [58]	Acoustic [58]

N.I. indicates Nano indentation. Bulk modulus was obtained through the conversion of Young's modulus with Poisson's ratio. DAC denotes Diamond anvil cells.

Comparing the values of the two systems studied, BT-648 exhibits a higher bulk modulus BT-649. This difference likely arises from two primary facts: (a) the binary constituents of the carbonitride system possess intrinsically higher bulk moduli, whereas the carbide system includes comparatively softer components, e.g., VC and NbC, (b) mixed carbon and nitrogen occupancy in the anionic sublattice may introduce bond heterogeneities that enhance lattice stiffness.
Additionally, bulk modulus values reported from diamond anvil cell (DAC) experiments may differ from those obtained using large-volume press (LVP) methods due to differences in stress states. Non-hydrostatic conditions in DAC experiments can lead to systematic overestimation or underestimation of bulk modulus values, while variations in pressure calibration methods further complicate direct comparison between DAC and LVP measurements.

3.3 High Temperature behavior at 0, 20 GPa

To evaluate the effect of pressure on thermal expansion, in-situ XRD measurements were first performed on BT-648 at ambient pressure from room temperature to 700 °C in air as a reference (Figure 6a and 6b). The ceramic remained stable as a single-phase carbonitride up to 600 °C, while further increases in temperature led to oxidation and the formation of compositionally complex oxide phases such as MO_2, M_2O_5, or mixed oxides such as $(Zr,Hf)_6(Nb,Ta)_2O_{17}$.[64] The Rietveld fit of

room temperature as representative refinement can be seen in Figure 6c and the fit parameters can be seen in Table 3.

Table 3. Fitting parameters of the Rietveld refined BT-648 obtained at 26 °C before initializing in-situ high temperature XRD measurement.

Sample	*Rp* (%)	*wRp* (%)	*Re* (%)	χ^2	*a* (Å)
(Ti,Zr,Hf,Nb,Ta)$C_{0.54}N_{0.4}$	27.6	20.0	14.6	1.89	4.38(1)

Under high-pressure conditions, material stability may be strongly influenced by reduced interatomic distances, whereas dislocation generation occurs through plastic deformation under deviatoric stress [65,66]. Increasing temperature under pressure may additionally promote phase transformations through structural rearrangements, coordination changes, or enhanced diffusion, as reported for systems such as Hf_3N_4 [54], or through sintering accompanied by dislocation annihilation and recrystallisation [61]. For both BT-648, and BT-649, gradual heating under pressure produced a pronounced increase in crystallinity, as shown in Figure 6d and 6e, indicating grain growth and partial dislocation recovery. Even at temperatures up to 1700 °C, neither composition exhibited detectable phase separation or structural transformation, thereby demonstrating high structural stability throughout the investigated HP–HT range.

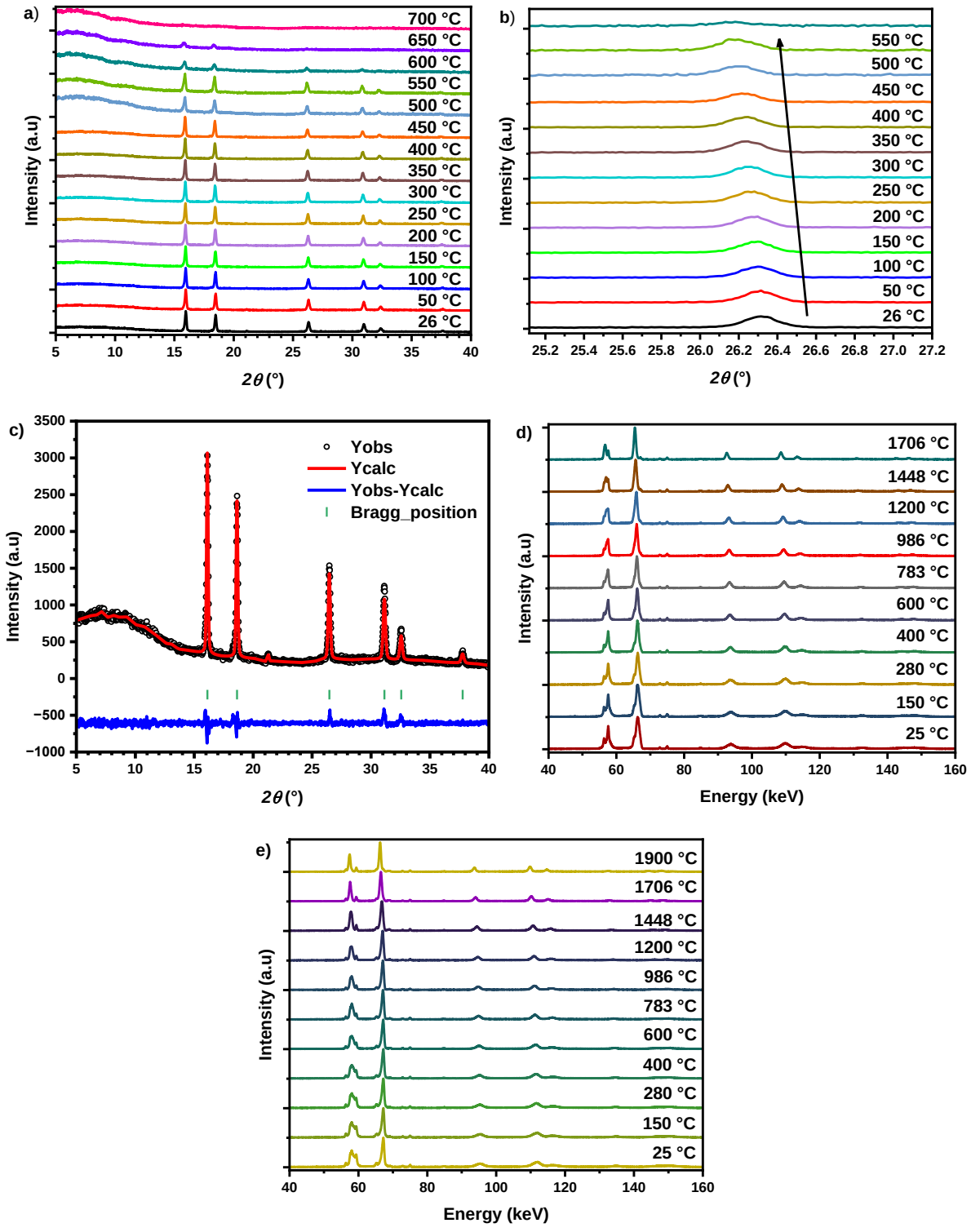

Figure 6. ED-XRD patterns of (a)In-situ diffractograms BT-648 at 0 GPa, (b) Inset of (220) indicating the lattice expansion with respect to temperature, (c) Rietveld refinement of BT-648 measured during in-situ HT XRD measurements, ED-XRD diffractograms of (d) BT-648, (e) BT-649 with respect to temperature at 20 GPa.

The volumetric thermal expansion at both ambient conditions and at high-pressure conditions was determined from the lattice parameters obtained through the Rietveld refinements and Le Bail refinements, respectively, based upon equations (5) and (6).

$$\alpha_V^P = \frac{1}{V}\left(\frac{dV}{dT}\right)_P \quad (5)$$

$$\ln(V^P) = \ln(V_{300}^P) + \int_{300}^{T} \alpha_V^P(T)dT \quad (6)$$

where α_V^P indicates the volumetric thermal expansion at constant pressure P, V denotes volume, V_{300}^P denotes volume at 300 K at pressure P (in this case, it is either 0 GPa or 20 GPa), V^P denotes recorded volume at constant pressure.

The results for both ceramics are shown in Figure 7a-d. It is clearly seen that the volumetric expansion of BT-648at 0 GPa is linear up to 873 K (600 °C), with α_V^0 = 2.58*10^{-5} /K, consistent with a quasi-harmonic behavior. At 20 GPa, the sample followed a quadratic dependence described by

$$\ln\left(\frac{V}{V_{300}}\right) = 5.97 * 10^{-6}(T - 300) + \frac{1}{2}(1.33 * 10^{-8})(T^2 - 300^2)$$

yielding α_V^{20} = 5.97*10^{-6}+1.33*10^{-8}T. The effect of pressure on thermal expansion is clearly seen, as the thermal expansion was suppressed to 61% of the ambient pressure value. BT-649 (Figure 7c-d) exhibited a similar trend to BT-648 with

$$V = 76.88 - 2.34 * 10^{-4}T + 9.72 * 10^{-7}T^2$$

$$\ln\left(\frac{V}{V_{300}}\right) = 2.84 * 10^{-6}(T - 300) + \frac{1}{2}(2.05 * 10^{-8})(T^2 - 300^2)$$

yielding α_V^{20} = 2.84*10^{-6}+2.05*10^{-8}T. The presence of the T^2 term indicates anharmonicity due to pressure, thereby resulting in thermal expansion as a function of temperature [63].

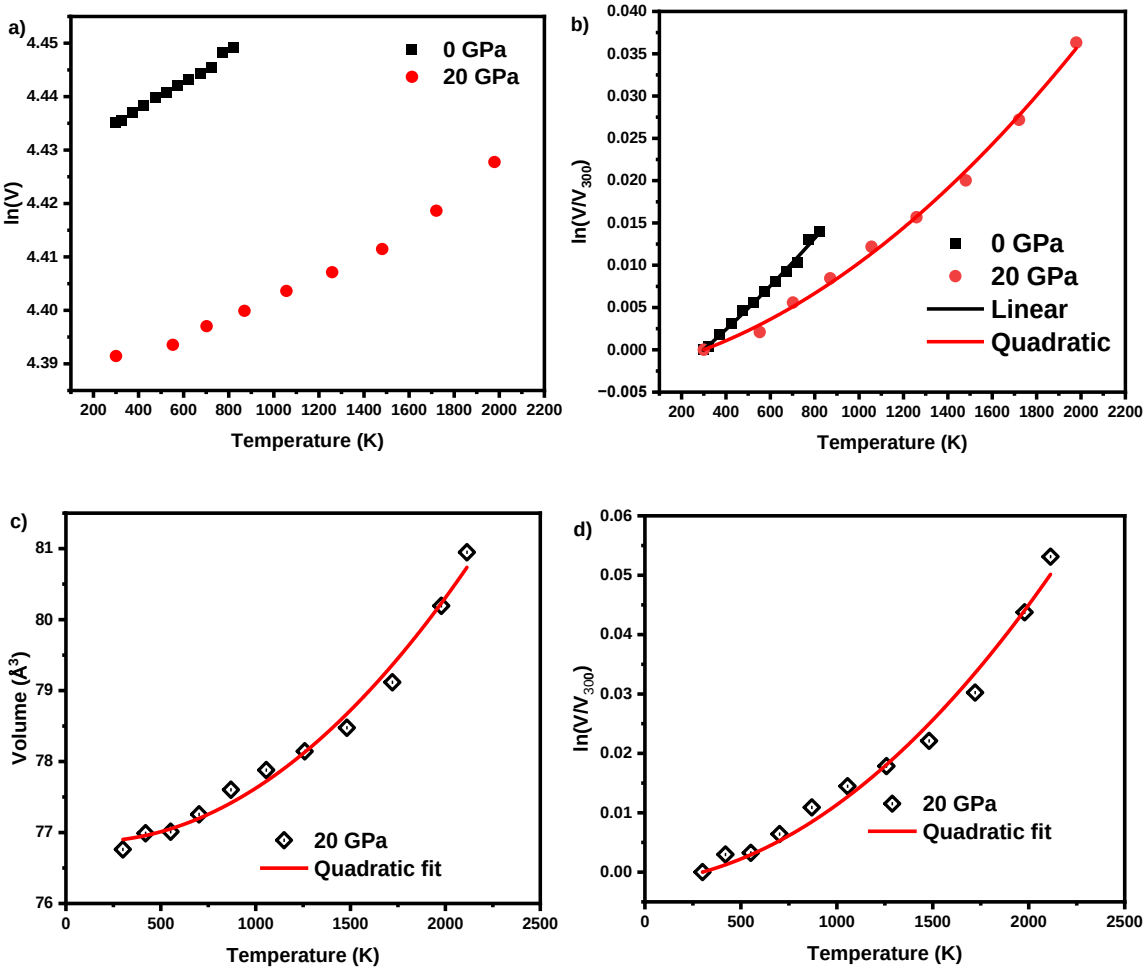

Figure 7. (a) Volumetric expansion at 0, 20 GPa for BT-648, (b) Fitting of BT-648, (c) Volumetric expansion of BT-649 at 20 GPa, (d) Fitting of volume expansion for BT-649.

The reason for such anharmonic thermal expansion lies within the asymmetry of the potential energy well of the ceramics. At lower temperatures, the asymmetry of the potential is minor, so the expansion is approximately linear with respect to temperature. With increasing pressure, the asymmetry is pronounced because ions are displaced into the steeper repulsive part of the potential energy curve. This leads to a non-linear increase in asymmetry with temperature, resulting in a quadratic dependence of expansion.

As the anharmonic behavior is reflected in both ceramics, this confirms that the quadratic nature is a pressure-driven phenomenon, and the anionic composition makes little contribution to it. In compositionally complex carbonitrides, the presence of M-C and M-N bonds with different bond lengths and bond constants contributes to local lattice asymmetry. The local lattice asymmetry, differences in bond character due to ionic vs. covalent bonding, and the presence of multiple elements lead to a distributed potential energy well and broaden the anharmonic behavior relative to carbide or nitride counterparts.

The post-experimental recovered samples were observed under SEM for their morphology and are shown in Figure 8a-d. The recovered samples clearly showed a high degree of compaction, as the pre-HP-HT samples are powders, as seen in Figure 8e.

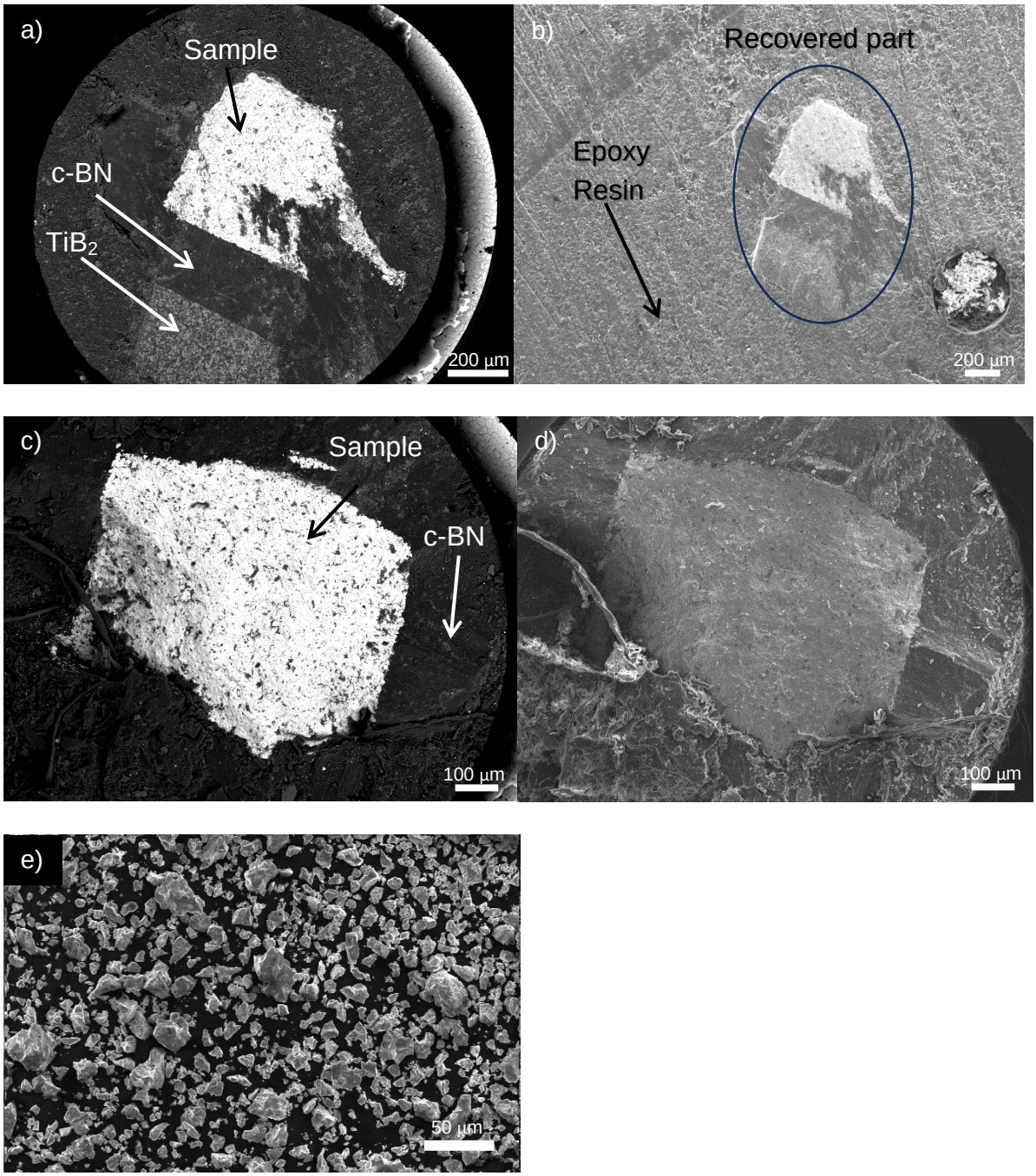

Figure 8. SEM of post HP-HT samples of (a) BT-648 in BSE mode, (b) BT-648 in SE mode, (b) BT-649 in BSE mode, and (d) BT-649 in SE mode, (e) BT-649 powders before high pressure high temperature.

4. Conclusions

In this work, two rock-salt-type compositions, (Ti,Zr,Hf,Nb,Ta)$C_{0.54}N_{0.4}$, and (V,Nb,Ta,Mo,W)$C_{0.8}$, were successfully synthesized through a non-oxidic sol-gel process assisted with high-temperature annealing at 1700 °C. The non-oxidic sol–gel route proved effective for producing compositionally complex nitride powders at temperatures as low as 1000 °C, offering a lower-temperature alternative to conventional spark plasma sintering (SPS)-based approaches. Pre-annealed ceramic contained minor oxide impurities, whereas the annealed samples are single-phase, although nitrogen loss occurred during high-temperature treatment.

The resulting ceramic powders were investigated for structural stability under combined high-pressure and high-temperature conditions by compression to 20 GPa followed by heating to 1900 °C while maintaining constant pressure. Internal pressure was determined using standard pressure marker mixtures, specifically Pt + KCl for (Ti,Zr,Hf,Nb,Ta)$C_{0.54}N_{0.4}$ and MgO + CsCl for (V,Nb,Ta,Mo,W)$C_{0.8}$.Both ceramics retained structural stability up to 20 GPa, and their lattice parameters were determined at selected intervals during compression.
The room-temperature bulk moduli were determined to be 309 GPa and 267 GPa, respectively, using the Birch–Murnaghan equation of state.
Furthermore, thermal stability under pressure was evaluated through stepwise heating to 1900 °C at 20 GPa. The absence of detectable phase transformation throughout this HP–HT range confirmed the high structural resilience of both compositions under the investigated conditions.
Pressure significantly influenced thermal expansion behavior, resulting in anharmonic volumetric expansion described by $\alpha_V^{20} = 5.97*10^{-6}+1.33*10^{-8}T$ (as for (Ti,Zr,Hf,Nb,Ta)$C_{0.54}N_{0.4}$), and $\alpha_V^{20} = 2.84*10^{-6}+2.05*10^{-8}T$ (as for (V,Nb,Ta,Mo,W)$C_{0.8}$).
The HP–HT large-volume press approach offers significant advantages over DAC methods by enabling larger sample volumes under quasi-hydrostatic conditions, thereby providing a robust platform for determining bulk moduli, thermal expansion behavior, and the synthesis or evaluation of new compositionally complex ceramic systems.

Acknowledgments

We acknowledge DESY (Hamburg, Germany), a member of the Helmholtz Association HGF, for the provision of experimental facilities. Parts of this research were carried out at beamline P61B (Proposal No. I-20211133). The beamline LVP instrument Aster-15 is funded by the ErUM-Pro programme (grants no.: 05K16WC2 & 05K13WC2) of the German Federal Ministry of Research, Technology, and Space (BMFTR). The SEM was performed with the aid of Laura Feldmann. The support of Dr. Robert Farla (DESY) during beam time and providing the necessary software for data analysis purposes is gratefully acknowledged.

References

[1] Z. Wen, Y. Liu, J. Yang, Y. Chen, Y. Fu, L. Zhuang, H. Yu, Y. Chu, Exceptional Oxidation Resistance of High-Entropy Carbides up to 3600 °C, Adv. Mater. 37 (2025) 2507254. https://doi.org/10.1002/adma.202507254.

[2] J. Li, Y. Zhang, Y. Zhao, Y. Zou, J. Lv, J. Li, A novel (Hf1/3Zr1/3Ti1/3)C medium-entropy carbide coating with excellent long-life ablation resistance applied above 2100 °C, Compos. Part B Eng. 251 (2023) 110467. https://doi.org/10.1016/j.compositesb.2022.110467.

[3] E. Castle, T. Csanádi, S. Grasso, J. Dusza, M. Reece, Processing and Properties of High-Entropy Ultra-High Temperature Carbides, Sci. Rep. 8 (2018) 8609. https://doi.org/10.1038/s41598-018-26827-1.

[4] Y. Wang, M.J. Reece, Oxidation resistance of (Hf-Ta-Zr-Nb)C high entropy carbide powders compared with the component monocarbides and binary carbide powders, Scr. Mater. 193 (2021) 86–90. https://doi.org/10.1016/j.scriptamat.2020.10.038.

[5] Y. Wang, B. Zhang, C. Zhang, J. Yin, M.J. Reece, Ablation behavior of (Hf-Ta-Zr-Nb)C high entropy carbide ceramic at temperatures above 2100 °C, J. Mater. Sci. Technol. 113 (2022) 40–47. https://doi.org/10.1016/j.jmst.2021.09.064.

[6] J.-W. Yeh, S.-K. Chen, S.-J. Lin, J.-Y. Gan, T.-S. Chin, T.-T. Shun, C.-H. Tsau, S.-Y. Chang, Nanostructured High-Entropy Alloys with Multiple Principal Elements: Novel Alloy Design Concepts and Outcomes, Adv. Eng. Mater. 6 (2004) 299–303. https://doi.org/10.1002/adem.200300567.

[7] C.M. Rost, E. Sachet, T. Borman, A. Moballegh, E.C. Dickey, D. Hou, J.L. Jones, S. Curtarolo, J.-P. Maria, Entropy-stabilized oxides, Nat. Commun. 6 (2015) 8485. https://doi.org/10.1038/ncomms9485.

[8] L. Feng, W.G. Fahrenholtz, G.E. Hilmas, Y. Zhou, Synthesis of single-phase high-entropy carbide powders, Scr. Mater. 162 (2019) 90–93. https://doi.org/10.1016/j.scriptamat.2018.10.049.

[9] T.J. Harrington, J. Gild, P. Sarker, C. Toher, C.M. Rost, O.F. Dippo, C. McElfresh, K. Kaufmann, E. Marin, L. Borowski, P.E. Hopkins, J. Luo, S. Curtarolo, D.W. Brenner, K.S. Vecchio, Phase stability and mechanical properties of novel high entropy transition metal carbides, Acta Mater. 166 (2019) 271–280. https://doi.org/10.1016/j.actamat.2018.12.054.

[10] X.-F. Wei, J.-X. Liu, F. Li, Y. Qin, Y.-C. Liang, G.-J. Zhang, High entropy carbide ceramics from different starting materials, J. Eur. Ceram. Soc. 39 (2019) 2989–2994. https://doi.org/10.1016/j.jeurceramsoc.2019.04.006.

[11] H. Chen, Z. Wu, M. Liu, W. Hai, W. Sun, Synthesis, microstructure and mechanical properties of high-entropy (VNbTaMoW)C5 ceramics, J. Eur. Ceram. Soc. 41 (2021) 7498–7506. https://doi.org/10.1016/j.jeurceramsoc.2021.07.063.

[12] Y. Wang, T. Csanádi, H. Zhang, J. Dusza, M.J. Reece, Synthesis, microstructure, and mechanical properties of novel high entropy carbonitrides, Acta Mater. 231 (2022) 117887. https://doi.org/10.1016/j.actamat.2022.117887.

[13] K. Vasanthakumar, R. Gorle, S. Ariharan, S.R. Bakshi, Novel single phase (Ti0.2W0.2Ta0.2Mo0.2V0.2)C0.8 high entropy carbide using ball milling followed by reactive spark plasma sintering, J. Eur. Ceram. Soc. 41 (2021) 6756–6762. https://doi.org/10.1016/j.jeurceramsoc.2021.06.009.

[14] X.Q. Han, N. Lin, A.Q. Li, J.Q. Li, Z.G. Wu, Z.Y. Wang, Y.H. He, X.Y. Kang, C. Ma, Microstructure and characterization of (Ti,V,Nb,Ta)(C,N) high-entropy ceramic, Ceram. Int. 47 (2021) 35105–35110. https://doi.org/10.1016/j.ceramint.2021.09.053.

[15] D. Demirskyi, T.S. Suzuki, K. Yoshimi, O. Vasylkiv, Synthesis and high-temperature properties of medium-entropy (Ti,Ta,Zr,Nb)C using the spark plasma consolidation of carbide powders, Open Ceram. 2 (2020) 100015. https://doi.org/10.1016/j.oceram.2020.100015.

[16] L. Wang, X. Cao, Z. Li, K. Peng, Z. Zhang, J. Zhang, G. Han, Synthesis and Oxidation behavior of Ti-Zr-Ta(Hf) high entropy carbide nanopowders by sol-gel method, Ceram. Int. 50 (2024) 52439-52450. https://doi.org/10.1016/j.ceramint.2024.10.095.

[17] B. Petrovičovà, W. Xu, M.G. Musolino, F. Pantò, S. Patanè, N. Pinna, S. Santangelo, C. Triolo, High-Entropy Spinel Oxides Produced via Sol-Gel and Electrospinning and Their Evaluation as Anodes in Li-Ion Batteries, Appl. Sci. 12 (2022). https://doi.org/10.3390/app12125965.

[18] H. Yang, S. Klemm, J. Müller, M.F. Bekheet, A. Gurlo, D.A.H. Hanaor, Synthesis of high-entropy carbides from multi-metal polymer precursors, J. Eur. Ceram. Soc. 43 (2023) 4233–4243. https://doi.org/10.1016/j.jeurceramsoc.2023.03.050.

[19] T. Jin, X. Sang, R.R. Unocic, R.T. Kinch, X. Liu, J. Hu, H. Liu, S. Dai, Mechanochemical-Assisted Synthesis of High-Entropy Metal Nitride via a Soft Urea Strategy, Adv. Mater. 30 (2018). https://doi.org/10.1002/adma.201707512.

[20] F. Li, Y. Lu, X.G. Wang, W. Bao, J.X. Liu, F. Xu, G.J. Zhang, Liquid precursor-derived high-entropy carbide nanopowders, Ceram. Int. 45 (2019) 22437–22441. https://doi.org/10.1016/j.ceramint.2019.07.244.

[21] B. Du, H. Liu, Y. Chu, Fabrication and characterization of polymer-derived high-entropy carbide ceramic powders, J. Am. Ceram. Soc. 103 (2020) 4063–4068. https://doi.org/10.1111/jace.17134.

[22] T. Xue, L. Xuefeng, H. Lei, H. Dai, Z. Huang, H. Zhang, One-step molten salt synthesis of high entropy oxides, Ceram. Int. 50 (2024) 18294–18302. https://doi.org/10.1016/j.ceramint.2024.02.313.

[23] S. Ning, T. Wen, B. Ye, Y. Chu, Low-temperature molten salt synthesis of high-entropy carbide powders, J. Am. Ceram. Soc. 103 (2019) 2244–2251. https://doi.org/10.1111/jace.16896.

[24] B. Ye, F. Che, H. Yangjie, M. Mengdong, C. Yanhui, Synthesis of high-entropy diboride nanopowders via molten salt-mediated magnesiothermic reduction, J. Am. Ceram. Soc. 103 (2020) 4738–4741. https://doi.org/10.1111/jace.17184.

[25] P. Sarker, T. Harrington, C. Toher, C. Oses, M. Samiee, J.-P. Maria, D.W. Brenner, K.S. Vecchio, S. Curtarolo, High-entropy high-hardness metal carbides discovered by entropy descriptors, Nat. Commun. 9 (2018) 4980. https://doi.org/10.1038/s41467-018-07160-7.

[26] P.M. Brune, G.E. Hilmas, W.G. Fahrenholtz, J.L. Watts, C.J. Ryan, C.M. DeSalle, D.E. Wolfe, S. Curtarolo, Hardness of single phase high entropy carbide ceramics with different compositions, J. Appl. Phys. 135 (2024) 165106. https://doi.org/10.1063/5.0198141.

[27] O.F. Dippo, N. Mesgarzadeh, T.J. Harrington, G.D. Schrader, K.S. Vecchio, Bulk high-entropy nitrides and carbonitrides, Sci. Rep. 10 (2020) 21288. https://doi.org/10.1038/s41598-020-78175-8.

[28] S. Guan, H. Liang, Q. Wang, L. Tan, F. Peng, Synthesis and Phase Stability of the High-Entropy Carbide (Ti0.2Zr0.2Nb0.2Ta0.2Mo0.2)C under Extreme Conditions, Inorg. Chem. 60 (2021) 3807–3813. https://doi.org/10.1021/acs.inorgchem.0c03319.

[29] S. Guan, W. Lin, H. Liang, W. Liang, Y. Tian, D. He, F. Peng, The effect of pressure tuning on the structure and mechanical properties of high-entropy carbides, Scr. Mater. 216 (2022) 114755. https://doi.org/10.1016/j.scriptamat.2022.114755.

[30] S. Iwan, M.S. Ahmad, C.C. Chen, S.A. Catledge, Y.K. Vohra, Experimental and

computational studies on high-entropy carbide MoNbTaVWC5 under high pressures, J. Appl. Phys. 138 (2025). https://doi.org/10.1063/5.0291488.

[31] H. Shu, W. Zhong, H. Zhao, F. Hong, B. Yue, Mechanical properties and high-pressure behavior of high entropy carbide (Mo, Nb, Ta, V, W)C, Int. J. Refract. Met. Hard Mater. 121 (2024) 106651. https://doi.org/10.1016/j.ijrmhm.2024.106651.

[32] D.T. Teppala, J. Bernauer, A. Rashid, M. Pejic, D. Zagorac, B. Matovic, E. Ionescu, Single-Source Precursor Synthesis of a Compositionally Complex Early Transitional Metal Carbonitride (Ti,Zr,Hf,Nb,Ta)NxC1−x, Adv. Eng. Mater. 26 (2024) 2302165. https://doi.org/10.1002/adem.202302165.

[33] D.T. Teppala, M. Pejić, D. Zagorac, E. Adabifiroozjaei, N. Goyal, L. Molina-Luna, S. Mathur, B. Matović, E. Ionescu, Single-source precursor synthesis of a compositionally complex early transitional metal nitride (V, Nb, Ta, Mo, W)Nx and its high temperature stability, Int. J. Appl. Ceram. Technol. 23 (2026) e70120. https://doi.org/10.1111/ijac.70120.

[34] J. Rodriguez-Carvajal, Fullprof: A program for Rietveld refinement and pattern matching analysis, Abstract of the Satellite Meeting on Powder Diffraction of the XV Congress of the IUCr, Toulouse, France, 1990, p. 127.

[35] R. Farla, S. Bhat, S. Sonntag, A. Chanyshev, S. Ma, T. Ishii, Z. Liu, A. Neri, N. Nishiyama, G.A. Faria, T. Wroblewski, H. Schulte-Schrepping, W. Drube, O. Seeck, T. Katsura, Extreme conditions research using the large-volume press at the P61B endstation, PETRA III, J. Synchrotron Radiat. 29 (2022) 409–423. https://doi.org/10.1107/S1600577522001047.

[36 M. Yokoo, N. Kawai, K.G. Nakamura, K. Kondo, Y. Tange, T. Tsuchiya, Ultrahigh-pressure scales for gold and platinum at pressures up to 550 GPa, Phys. Rev. B. 80 (2009) 104114. https://doi.org/10.1103/PhysRevB.80.104114.

[37] S. Tateno, T. Komabayashi, K. Hirose, N. Hirao, Y. Ohishi, Static compression of B2 KCl to 230 GPa and its P-V-T equation of state, Am. Mineral. 104 (2019) 718–723. https://doi.org/10.2138/am-2019-6779.

[38] Y. Tange, Y. Nishihara, T. Tsuchiya, Unified analyses for P-V-T equation of state of MgO: A solution for pressure-scale problems in high P-T experiments, J. Geophys. Res. Solid Earth. 114 (2009). https://doi.org/10.1029/2008JB005813.

[39] A. Dewaele, Compression of CsCl and CsBr in the megabar range, High Press. Res. 40 (2020) 402–410. https://doi.org/10.1080/08957959.2020.1774754.

[440 Y. Seto, D. Nishio-Hamane, T. Nagai, N. Sata, Development of a Software Suite on X-ray Diffraction Experiments, Rev. High Press. Sci. Technol. 20 (2010) 269–276. https://doi.org/10.4131/jshpreview.20.269.

[41] B.H. Toby, R.B. Von Dreele, GSAS-II: the genesis of a modern open-source all purpose crystallography software package, J. Appl. Crystallogr. 46 (2013) 544–549. https://doi.org/10.1107/S0021889813003531.

[42] J. Gonzalez-Platas, M. Alvaro, F. Nestola, R. Angel, EosFit7-GUI: a new graphical user interface for equation of state calculations, analyses and teaching, J. Appl. Crystallogr. 49 (2016) 1377–1382. https://doi.org/10.1107/S1600576716008050.

[43] R.D. Deslattes, E.G. Kessler, P. Indelicato, L. de Billy, E. Lindroth, J. Anton, X-ray transition energies: new approach to a comprehensive evaluation, Rev. Mod. Phys. 75 (2003) 35–99. https://doi.org/10.1103/RevModPhys.75.35.

[44] N.A. Dubrovinskaia, L.S. Dubrovinsky, S.K. Saxena, R. Ahuja, B. Johansson, High-pressure study of titanium carbide, J. Alloys Compd. 289 (1999) 24–27. https://doi.org/10.1016/S0925-8388(99)00159-0.

[45] L. Xiong, B. Li, B. Liang, J. Zhu, H. Yi, J. Zhang, A high-pressure study of HfC and nano-

crystalline TiC by X-ray diffraction and density functional theory calculations, Mod. Phys. Lett. B. 34 (2020) 2050393. https://doi.org/10.1142/S0217984920503935.

[46] L. Tan, Z. Zeng, H. Lou, F. Zhang, X. Chen, S. Chen, Y. Xuan, F. Peng, Q. Zeng, Stability of Zirconium Carbide under High Pressure and High Temperature, J. Phys. Chem. C. 123 (2019) 10051–10056. https://doi.org/10.1021/acs.jpcc.9b00715.

[47] R. He, L. Fang, T. Han, G. Yang, G. Ma, J. Liu, X. Chen, L. Xie, L. Liu, Q. Li, Y. Tang, H. Liang, Y. Zou, F. Peng, Elasticity, mechanical and thermal properties of polycrystalline hafnium carbide and tantalum carbide at high pressure, J. Eur. Ceram. Soc. 42 (2022) 5220–5228. https://doi.org/10.1016/j.jeurceramsoc.2022.06.039.

[48] H.P. Liermann, A.K. Singh, B. Manoun, S.K. Saxena, V.B. Prakapenka, G. Shen, Compression behavior of VC0.85 up to 53 GPa, Int. J. Refract. Met. Hard Mater. 22 (2004) 129–132. https://doi.org/10.1016/j.ijrmhm.2004.02.001.

[49] H.P. Liermann, A.K. Singh, M. Somayazulu, S.K. Saxena, Compression behavior of NbC under nonhydrostatic conditions to 57GPa, Int. J. Refract. Met. Hard Mater. 25 (2007) 386–391. https://doi.org/10.1016/j.ijrmhm.2006.12.002.

[50] H. Chen, Y. Bi, H. Mao, J. Xu, L. Liu, Q. Jing, Z. Li, X. Chen, Q. Wang, High-pressure strength of nanocrystalline tantalum carbide (TaC) studied at a non-hydrostatic compression, Int. J. Refract. Met. Hard Mater. 41 (2013) 627–630. https://doi.org/10.1016/j.ijrmhm.2013.04.009.

[51] J. Haines, J.M. Léger, C. Chateau, J.E. Lowther, Experimental and theoretical investigation of Mo2C at high pressure, J. Phys. Condens. Matter. 13 (2001) 2447. https://doi.org/10.1088/0953-8984/13/11/303.

[52] Q. Fan, H. Hou, J. Yang, Pressure induced structural, mechanical and thermodynamic properties of W2C, Int. J. Refract. Met. Hard Mater. 123 (2024) 106745. https://doi.org/10.1016/j.ijrmhm.2024.106745.

[53] Q. Wang, D. He, F. Peng, L. Xiong, J. Wang, P. Wang, C. Xu, J. Liu, Compression behavior of nanocrystalline TiN, Solid State Commun. 182 (2014) 26–29. https://doi.org/10.1016/j.ssc.2013.12.015.

[54] A. Zerr, G. Miehe, R. Riedel, Synthesis of cubic zirconium and hafnium nitride having Th3P4 structure, Nat. Mater. 2 (2003) 185–189. https://doi.org/10.1038/nmat836.

[55] L. Xiong, L. Huang, D. Liu, Y. Ding, J. Zhang, Effect of pressure on vanadium nitride using XRD and DFT, High Press. Res. 43 (2023) 58–67. https://doi.org/10.1080/08957959.2023.2191195.

[56] H. Yusa, F. Kawamura, T. Taniguchi, N. Hirao, Y. Ohishi, T. Kikegawa, High-pressure synthesis and compressive behavior of tantalum nitrides, J. Appl. Phys. 115 (2014) 103520. https://doi.org/10.1063/1.4867986.

[57] Q. Li, Y. Li, Y. Wang, H. Liang, X. Li, J. Sun, Y. Zou, Boosting the strength and toughness of (TiZrNbTa)C0.8N0.2 carbonitride via high-entropy and high-pressure engineering, Appl. Mater. Today. 48 (2026) 103012. https://doi.org/10.1016/j.apmt.2025.103012.

[58] T. Wen, B. Ye, M.C. Nguyen, M. Ma, Y. Chu, Thermophysical and mechanical properties of novel high-entropy metal nitride-carbides, J. Am. Ceram. Soc. 103 (2020) 6475–6489. https://doi.org/10.1111/jace.17333.

[59] L. Ran, S. Guan, W. Liang, J. Pu, P. He, H. Long, P. Yang, F. Peng, The phase diagram and strengthening behavior of compositionally complex carbides under high pressure, J. Am. Ceram. Soc. 108 (2025) 1–9. https://doi.org/10.1111/jace.20368.

[60] V. Suvorova, D. Suvorov, S. Volodko, M. Poliakov, L. Volkova, A. Nepapushev, D. Moskovskikh, High-entropy carbonitrides with superior oxidation resistance: Fabrication and

investigation of oxidation behavior under non-isothermal and isothermal conditions, J. Eur. Ceram. Soc. 45 (2025). https://doi.org/10.1016/j.jeurceramsoc.2024.116980.

[61] H. Liang, L. Fang, S. Guan, F. Peng, Z. Zhang, H. Chen, W. Zhang, C. Lu, Insights into the Bond Behavior and Mechanical Properties of Hafnium Carbide under High Pressure and High Temperature, Inorg. Chem. 60 (2021) 515–524. https://doi.org/10.1021/acs.inorgchem.0c02800.

[62] H. Liang, W. Lin, L. Fang, S. Guan, Q. Wang, W. Wang, Z. Fan, L. Liu, J. Kai, F. Peng, C. Lu, Achieving Dislocation Strengthening in Hafnium Carbide through High Pressure and High Temperature, J. Phys. Chem. C. 125 (2021) 24254–24262. https://doi.org/10.1021/acs.jpcc.1c08086.

[63] X.G. Lu, M. Selleby, B. Sundman, Calculations of thermophysical properties of cubic carbides and nitrides using the Debye-Grüneisen model, Acta Mater. 55 (2007) 1215–1226. https://doi.org/10.1016/j.actamat.2006.05.054.